RESEARCH ARTICLE

Enhanced nonlinear optical response and ultrafast carrier dynamics in amorphous Fe-doped ZIF-67

Linghao Kong,†[a] Yunkai Sun,†[b] Hongwei Chu, [ID] *[a] Shiping Xu, [ID] [b] Zhongben Pan,[a] Han Pan, [ID] [a] Shengzhi Zhao[a] and Dechun Li [ID] *[a]

Developing novel materials with excellent nonlinear optical response and ultrafast carrier dynamics is of great significance for the development of optoelectronic devices. In this contribution, amorphous Fe-doped ZIF-67 (Fe-ZIF-67) was successfully synthesized and characterized in detail. Femtosecond-resolved transient absorption spectroscopy (TAS) clearly revealed the ultrafast carrier dynamics of Fe-ZIF-67 and ZIF-67. The results showed that amorphous Fe-ZIF-67 exhibited a deeper photoinduced bleaching valley and a higher photoinduced absorption peak when compared with the crystalline ZIF-67. Meanwhile, the introduction of Fe ions promoted the charge transfer in ZIF-67 and significantly inhibited the photogenerated carrier recombination, thus greatly enhancing the nonlinear optical response of Fe-ZIF-67. This indicates its great potential in nonlinear optical applications. In addition, amorphous Fe-ZIF-67 displayed excellent nonlinear saturation absorption features at 1.5 μm, with a modulation depth of 3.1% and a saturation light intensity of 1.84 MW cm^{-2}. Subsequently, Fe-ZIF-67 was inserted into an erbium-doped fiber ring cavity to generate conventional soliton mode-locking laser pulses with a pulse width of 1.23 ps and a wavelength of 1560.8 nm. Surprisingly, the harmonic order of mode locking could be tuned by adjusting the polarization controller (PC), which is different from the previously known method of adjusting the pump power. Finally, a 95th-order harmonic mode-locking pulse output was obtained with a repetition rate of 694.8 MHz. Compared to the crystalline ZIF-67 saturable absorber (SA), amorphous Fe-ZIF-67 SA increased the mode-locking frequency to the order of several hundred megahertz. Therefore, it is of great significance to synthesize amorphous advanced MOF functional materials by changing the crystal structure through doping and to further investigate their feasibility for application in the field of optoelectronics.

Introduction

Amorphous materials can extensively exist in intermetallic compounds, inorganic materials, and organic materials.[1–4] Unlike crystalline materials with long-range ordering, the internal atomic arrangement of amorphous materials is not periodic, allowing only local short-range ordering, so there are large numbers of randomly oriented bonds, making amorphous materials with abundant defects and active sites.[5,6] Furthermore, due to their superb properties such as high electrical conductivity, low resistivity, high strength, and extreme hardness, amorphous materials are widely used in electronics, aerospace, machinery, and other fields. In recent years, the scientific community's research on amorphous materials has been extended to metal–organic frameworks (MOFs) made of metal atoms connected by organic ligands into crystal arrays.[7,8] Research shows that amorphous MOFs, as a new class of materials, often possess rich functional behaviors due to their structural complexity.[9,10] Specifically, amorphous MOFs retain the local structural unit of their crystalline counterparts, but do not have the long-range order, and show better performance and broader application prospects than their crystalline counterpart in trapping harmful guest species,[11] improving ion transport capacity,[12] regulating drug delivery,[13] enhancing oxygen evolution reaction performance as a catalyst,[14] and improving photoluminescence efficiency.[15]

As a subclass of MOFs, zeolitic imidazolate frameworks (ZIFs) are composed of a negatively charged imidazolate ligand (im$^-$) combined with a tetrahedral coordination bivalent cation ($M^{2+} = Zn^{2+}$ or Co^{2+}).[16] Due to their permanent porosity and remarkable thermochemical stability, they have been extensively explored in the fields such as gas adsorption/storage,[17] batteries,[18] sensors,[19] molecular separations,[20,21] and catalysts.[22,23] In addition, the close structural similarities between ZIFs and zeolitic silica polymorphs make ZIFs an attractive candidate for

[a] School of Information Science and Engineering, Shandong University, Qingdao 266237, China. E-mail: hongwei.chu@sdu.edu.cn, dechun@sdu.edu.cn

[b] School of Environmental Science and Engineering, Shandong University, Qingdao 266237, China

† L. K. and Y. S. contributed equally to this work.

amorphization.[4,24,25] At present, inorganic zeolites can be transformed into amorphous structures under pressure or temperature.[26] Moreover, amorphous counterparts have also been reported to be obtained by structural collapse or melt quenching of the crystal parent material.[9] Among the many ZIF materials, ZIF-67 stands out because of its good thermal stability, large specific surface area, and excellent physical properties.[27] On the other hand, ZIF-67 exhibits the prominent nonlinear saturation absorption effect and can exist stably in the aqueous phase and most organic solvents. Inspired by the above facts, we selected crystalline ZIF-67 as the precursor and successfully changed the crystalline ZIF-67 into amorphous Fe-ZIF-67 through Fe ion doping and high-temperature calcination. Because Fe ions and Co ions in ZIF-67 are adjacent in the periodic table, with similar physical and chemical properties, and the similar ionic radius leads to easier doping into ZIF-67. Besides, Fe ions have the polyvalent property, resulting in lattice defects and oxygen vacancies during doping.[28] Therefore, it is regarded as an ideal doping material.

In this paper, the ordered structure and electron configuration of ZIF-67 were effectively adjusted *via* Fe doping, so amorphous Fe-ZIF-67 was successfully prepared. Then, we characterized the morphology, elemental composition, valence state, and crystallinity of Fe-ZIF-67. These results indicate that Fe elements were successfully doped into crystalline ZIF-67 to

form the amorphous Fe-ZIF-67. Additionally, the carrier dynamics in Fe-ZIF-67 and ZIF-67 were investigated by using the ultrafast TAS. The fast response time of Fe-ZIF-67 demonstrates its great potential for generating ultrashort pulses in continuous wave mode-locking. Then, Fe-ZIF-67 was deposited on the tapered fiber, and the modulation depth of 3.1% and the saturable intensity of 1.84 MW cm^{-2} were measured. By inserting Fe-ZIF-67 into the erbium-doped fiber ring cavity and adjusting the pump power to 185.5 mW, the conventional soliton mode-locking with a wavelength of 1560.8 nm, a pulse width of 1.23 ps and a repetition frequency of 7.31 MHz can be achieved. When the pump power was increased to 387 mW, the soliton cluster pulse and the 95-order harmonic mode-locking with the highest frequency of 694.8 MHz appeared after optimizing the polarization state in the resonator. This work indicates that amorphous Fe-ZIF-67 with excellent nonlinear optical properties may serve as a new alternative material for ultrafast photonics in the future.

Preparation and characterization of amorphous Fe-ZIF-67

The precursor solution of Fe was obtained by dissolving 0.6 g of Fe(NO$_3$)$_3$·9H$_2$O into 10 ml of methanol solution. 1 g of the purple ZIF-67 powder was dispersed in 30 ml of methanol
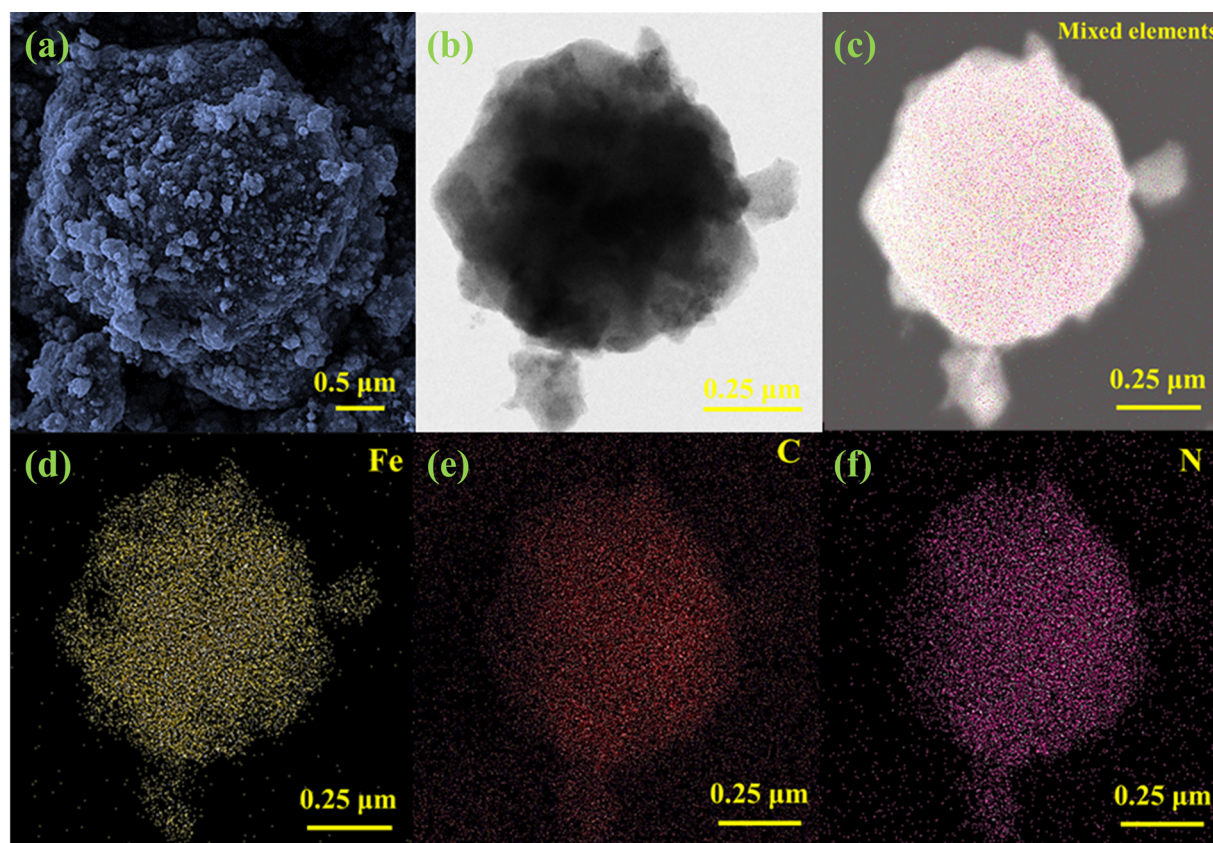
Fig. 1 (a) SEM image; (b) TEM image; (c) EDS element mapping images; (d) corresponding Fe element distribution; (e) corresponding C element distribution; (f) corresponding N element distribution.
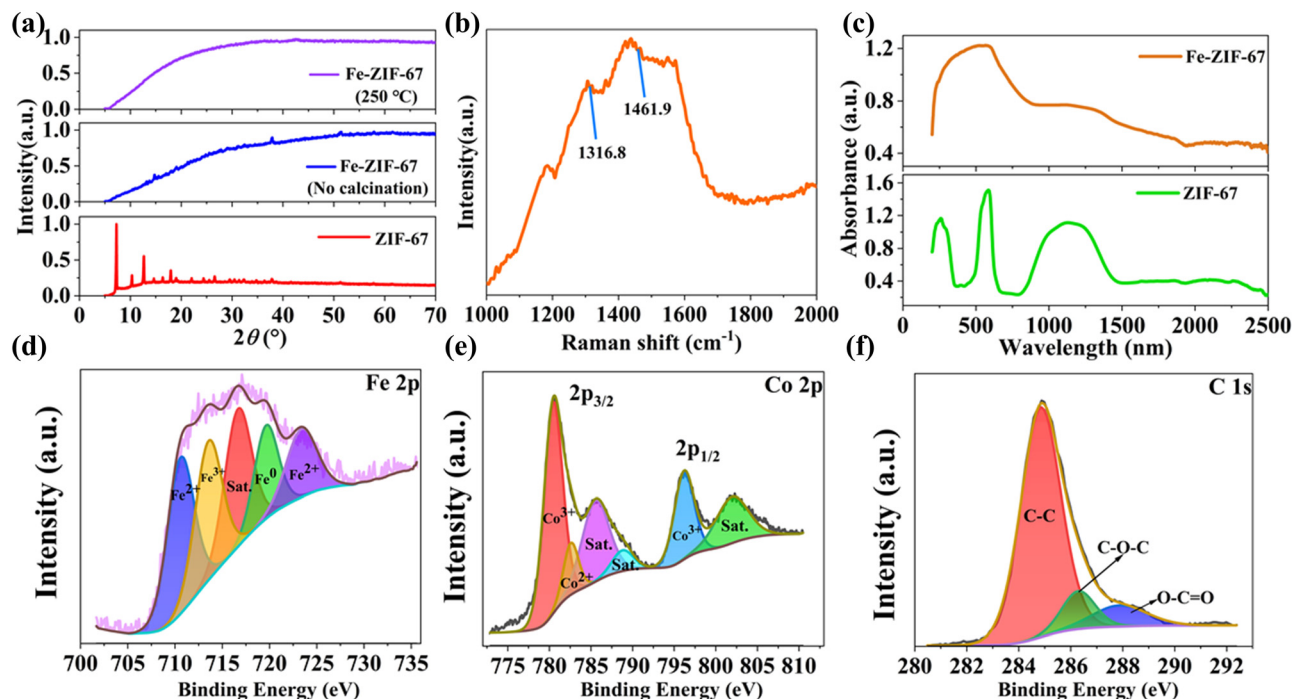
Fig. 2 (a) XRD pattern of ZIF-67 and Fe-ZIF-67; (b) Raman spectrum of Fe-ZIF-67; (c) UV-VIS-NIR absorption spectrum of ZIF-67 and Fe-ZIF-67; (d) Fe 2p spectrum of Fe-ZIF-67; (e) Co 2p spectrum of Fe-ZIF-67; (f) C 1s spectrum of Fe-ZIF-67.

solution to make it evenly dispersed so that we can obtain the ZIF-67 methanol solution. Then, the precursor solution of Fe was fully mixed with the ZIF-67 solution, ultrasonicated for 15 minutes, and magnetically stirred for 4 hours, and the mixed solution was heated and dried in a water bath of 100 °C. The collected solid samples were placed in a drying oven at a temperature of 60 °C overnight. Finally, the dried sample was placed in a tube furnace, heated to 250 °C at a heating rate of 5 °C min^{-1}, calcined for 5 hours, and then cooled to room temperature to obtain amorphous black Fe-ZIF-67.

To prove the validity of the prepared sample, we performed a series of characterizations on it. Fig. 1(a) shows a scanning electron microscope (SEM) image of Fe-ZIF-67. From the figure, we can see that some fine particles were attached to the rough surface of the sample. Although the sample maintains the morphology of ZIF-67, the regular structure of ZIF-67 has collapsed. The rough surface and collapsed structure of the sample are conducive to full interaction with the signal laser. The transmission electron microscope (TEM) image of Fe-ZIF-67 is shown in Fig. 1(b), and Fe-ZIF-67 generally retains the rhombohedral shape of ZIF-67, which is consistent with the SEM characterization. The energy dispersive spectrum (EDS) of Fe-ZIF-67 measured using a scanning transmission electron microscope (STEM) at a 250 nm resolution is shown in Fig. 1(c)–(f). Fig. 1(c) is the mixed element mapping diagram of Fe-ZIF-67. Fig. 1(d)–(f) show the element distribution mapping of the doped elements Fe, C and N in ZIF-67, respectively. The results indicate that Fe, C, and N elements are uniformly distributed in the sample, and Fe ions were successfully doped into ZIF-67.

To analyze the crystal structure of Fe-ZIF-67, X-ray diffraction (XRD) characterization was performed. As shown in Fig. 2(a), pure ZIF-67 has a sharp diffraction peak, indicating that ZIF-67 has excellent crystallinity. Under the condition of no calcination, the doping of Fe elements converts most of the crystalline ZIF-67 into amorphous Fe-ZIF-67, but still remains part of the crystallization of ZIF-67. All diffraction peaks of Fe-ZIF-67 obtained by calcination at 250 °C in a tube furnace disappear, so the prepared Fe-ZIF-67 is completely amorphous. This also fully indicates that it is an effective strategy to convert crystalline ZIF-67 into amorphous Fe-ZIF-67 by doping Fe and calcination to adjust the electronic configuration and destroy the original crystal structure of the material. The Raman spectra obtained at 532 nm emission are shown in Fig. 2(b), where the Raman peaks at 1316.8 cm^{-1} and 1461.9 cm^{-1} correspond to ZIF-67.[29] These wide and weak Raman peaks further confirm that Fe-ZIF-67 was amorphous. The absorption characteristics of Fe-ZIF-67 and ZIF-67 in the wavelength range of 200–2500 nm were measured by ultraviolet-visible-near infrared (UV-VIS-NIR) spectroscopy. As shown in Fig. 2(c), the introduction of Fe ions changes the absorption peak of ZIF-67 into a wide unbiased absorption band, possibly because the charge transfer between Fe and ZIF-67 reduces the valence electron transition between different excited states in ZIF-67. At 1.5 μm waveband, Fe-ZIF-67 has an absorption coefficient (0.63) about twice that of ZIF-67 (0.37), which has the potential to generate ultrafast pulses as a SA in the Erbium-doped fiber laser (EDFL). To further characterize the elemental composition, chemical state, and molecular structure of Fe-ZIF-67, X-ray photoelectron spectroscopy (XPS) was implemented. Fig. 2(d)
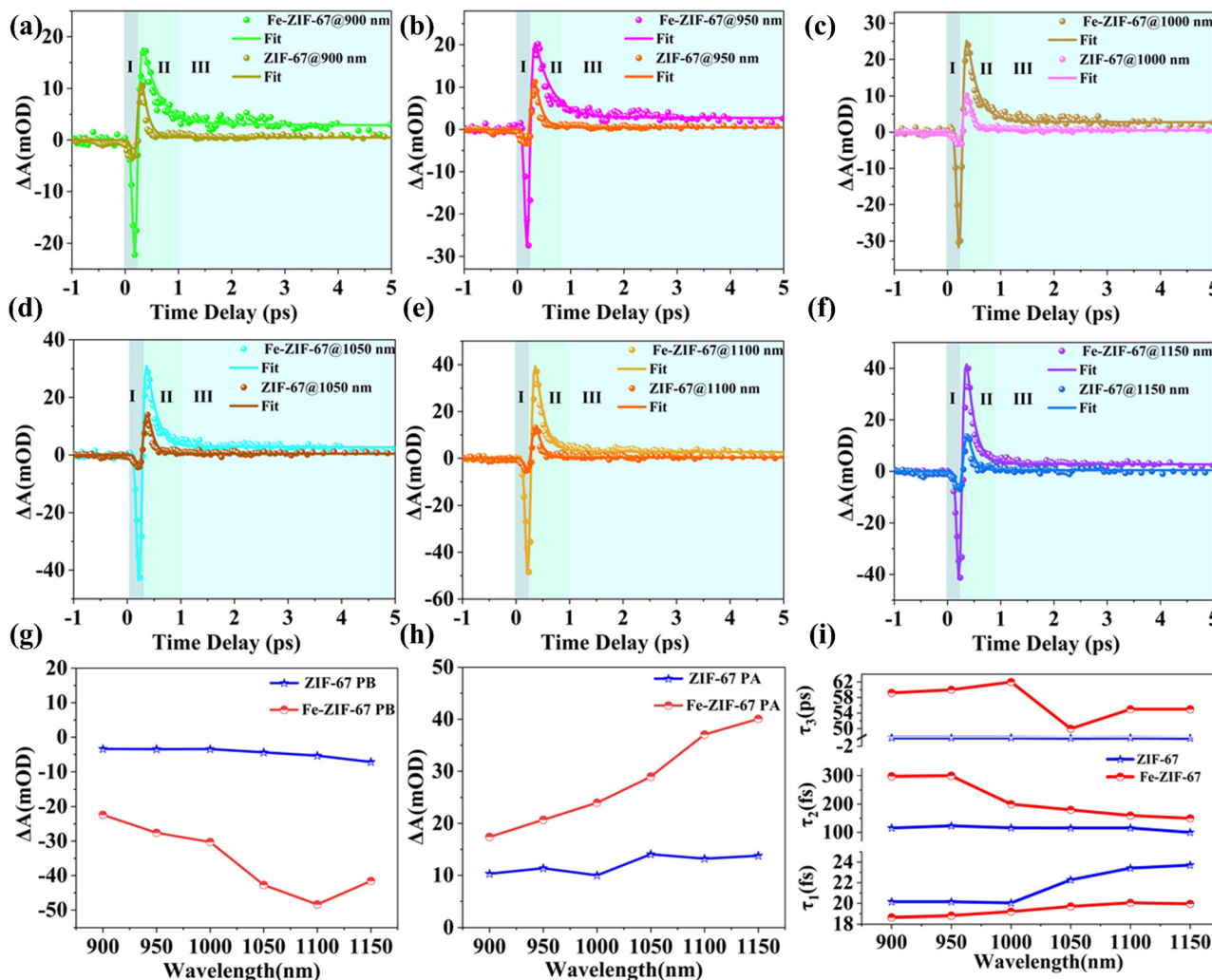
Fig. 3 (a–f) The dynamic curves of Fe-ZIF-67 and ZIF-67 at 900–1150 nm; (g) the PB values of Fe-ZIF-67 and ZIF-67 vary with the wavelength; (h) the PA values of Fe-ZIF-67 and ZIF-67 vary with the wavelength; (i) lifetime fitting of Fe-ZIF-67 and ZIF-67 at different wavelengths.

shows the XPS spectrum of Fe 2p, which can be decomposed into five peaks, among which the peaks at 710.6 eV and 723.38 eV correspond to Fe^{2+},[30] the peak at 713.55 eV corresponds to the peak of Fe^{3+} $2p_{3/2}$,[31] 716.67 eV corresponds to the satellite peak,[32] and the peak at 719.64 eV comes from elemental Fe^0.[33] This shows that the Fe element in Fe-ZIF-67 mainly exists in the form of +2 and +3. The Co 2p spectrum of Fe-ZIF-67 is shown in Fig. 2(e), where the Co $2p_{3/2}$ peak is the main peak and the Co $2p_{1/2}$ peak is the shoulder peak. Co $2p_{3/2}$ consists of Co^{3+} with a binding energy of 780.4 eV,[34] Co^{2+} with a binding energy of 782.6 eV,[35] and two satellite peaks with a binding energy of 785.5 eV and 788.8 eV.[35,36] Co $2p_{1/2}$ is composed of Co^{3+} (796.18 eV) and satellite peak (802 eV).[35] As shown in Fig. 2(f), the XPS spectrum of C 1s can be decomposed into three different components, corresponding to C–C (284.8 eV), C–O–C (286.2 eV), and O–C=O (288.4 eV).[37] Thus, according to the above characterization results, it was further confirmed that the Fe element was successfully doped into ZIF-67.

To better explore the carrier dynamics of Fe-ZIF-67 and ZIF-67, the carrier recovery process was measured by femtosecond-resolved transient absorption spectroscopy. Pump light with a wavelength of 400 nm efficiently excites electrons, and wideband white light of 800 to 1200 nm is used to probe light. Fig. 3(a)–(f) compares the variation of ΔA with the pump–probe delay time τ of Fe-ZIF-67 and ZIF-67 when the probe wavelength λ is 900–1150 nm under exactly the same pumping conditions. ΔA is the absorption difference of the sample with or without pumped laser excitation and is used to reveal the high/low excited state absorption intensity. As shown in Fig. 3(a)–(f), the whole transient absorption process of Fe-ZIF-67 and ZIF-67 can be divided into three parts. Process I is a symmetric peak with negative ΔA and a duration of about 250 fs. ΔA rapidly drops to a negative valley value in process I, because the electrons of the ground state absorption pump light transition to the excited state, resulting in a decrease in the population of the ground state electrons, an increase in the population of the excited state electrons, and the absorption of the excited sample to the probe light is less than that of the unexcited sample to the probe light, that is, photoinduced bleaching (PB).[38] In the subsequent II process in the range of about 0.5 ps, ΔA gradually

increases to a positive value and a maximum peak appears. This maximum peak is called the photoinduced absorption (PA) peak and can be attributed to the hot carrier's relaxation and thermalization process or excited-state absorption.[38–40] Subsequently, ΔA in region III dropped rapidly from its maximum and remained essentially constant thereafter. This long recovery process in region III is mainly attributed to the Auger recombination process.[41] From Fig. 3(a)–(f), there is a strong PA signal at the probe wavelength of 900–1200 nm, which is consistent with the strong absorption of Fe-ZIF-67 and ZIF-67 in the UV-VIS-NIR absorption spectrum shown in Fig. 2(c). On the other hand, the PB signal presented by TAS indicates the broadband saturable absorption characteristics of Fe-ZIF-67 and ZIF-67. Fig. 3(g) and (h) summarize the change of the PB valley and PA peak of the transient absorption response of Fe-ZIF-67 and ZIF-67 with the probe wavelength. The PB valley and PA peaks of Fe-ZIF-67 and ZIF-67 showed an enhanced trend with the redshift of the probe wavelength. Compared with ZIF-67, Fe-ZIF-67 has a deeper PB valley and a higher PA peak, and the enhancement trend is more obvious, which indicates that Fe-ZIF-67 has stronger photoabsorption and photobleaching ability. This also indicates that the carrier density in Fe-ZIF-67 is higher than that of pure ZIF-67, its saturable absorption capacity is stronger, and then its nonlinear optical properties are better. The TAS curve shown in Fig. 3(a)–(f) is fitted with a three-exponential decay function in eqn (1):

$$\Delta A = A_1 \cdot \exp(-t/\tau_1) + A_2 \cdot \exp(-t/\tau_2) + A_3 \cdot \exp(-t/\tau_3) \quad (1)$$

where A_1, A_2, and A_3 are the first, second, and third amplitude terms, t is the delay time between the pump and probe light, and τ_1, τ_2, and τ_3 represent the response time of each process, respectively. The evolution of fitted τ_1, τ_2, and τ_3 of Fe-ZIF-67 and ZIF-67 with the increase of wavelength is shown in Fig. 3(h). It can be unambiguously seen that in the range of transient absorption response at 900–1150 nm, τ_1 of Fe-ZIF-67 is smaller than that of ZIF-67, and τ_2 and τ_3 are bigger than that of ZIF-67, indicating that the ground state bleaching feature of Fe-ZIF-67 takes a shorter time to reach saturation and then exhibits a slower decay rate. This shows that hole transfer is enhanced and charge recombination is reduced.[42] The photobleaching valley of Fe-ZIF-67 over a very short time scale determines its excellent performance for optical modulators and ultrafast lasers. As for the relaxation time τ_3, it can be seen in process III of Fig. 3(a)–(f) that Fe-ZIF-67 exhibits a slower decay process with ΔA of 2.9, while ZIF-67 remains at ~ 0.45. τ_3 of Fe-ZIF-67 is significantly higher than that of ZIF-67, mainly because the introduction of Fe ions leads to a new defect trap in ZIF-67, which effectively promotes the charge transfer process and significantly inhibits the photogenerated carrier recombination. Indeed, the promotion of charge transfer and the inhibition of photogenerated carrier recombination can achieve a substantial enhancement of the nonlinear optical response of the material.[43] The enhancement of nonlinear optical response in Fe-ZIF-67 is expected to result in more mode-locking states and more exciting performance parameters in erbium-doped fiber mode-locking cavities.[44,45]
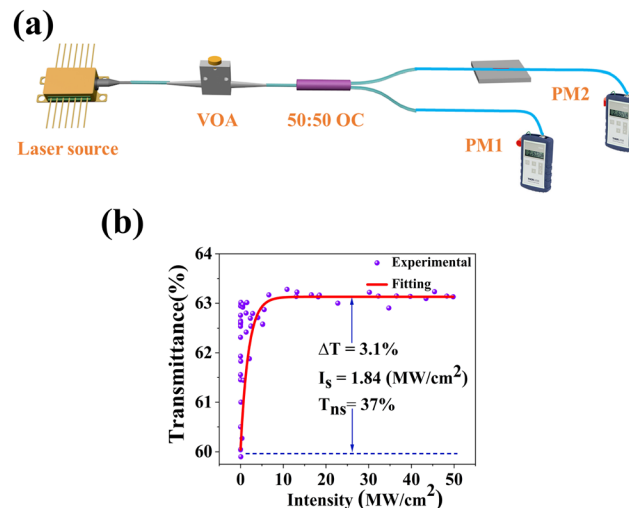

Fig. 4 (a) Installation diagram of Fe-ZIF-67 saturation absorption curve measurement system; (b) the nonlinear transmittance curve.

The nonlinear absorption characteristics of amorphous Fe-ZIF-67 were measured using a self-built twin-balanced detector system. The schematic diagram is shown in Fig. 4(a). The center wavelength of the self-made pulsed laser source is 1556 nm, the pulse width is 1.1 ps, and the fundamental frequency is 12.93 MHz. A variable optical attenuator (VOA) is used to adjust the power of the incident light that excites the saturable absorption response of the material. A 50:50 output coupler (OC) divides the beam into two equal parts, one of which acts as a reference light and the other passes through the Fe-ZIF-67 SA, the power ratio is the transmittance T. Fig. 4(b) shows the experimental results of the measured transmittance varying with the laser intensity. With the increase of the incident light intensity, the transmittance increases rapidly and tends to saturation. The transmittance curve was fitted by eqn (2):[46]

$$T = 1 - \Delta T \cdot \exp(-I/I_s) - T_{ns} \quad (2)$$

where ΔT, I_s, and T_{ns} are the modulation depth, saturation intensity, and nonsaturable loss, respectively. The fitted ΔT of 3.1%, I_s of 1.84 MW cm^{-2}, and T_{ns} of 37% indicate the potential of Fe-ZIF-67 SA to achieve pulsed laser output at 1.5 μm. In particular, the extremely low saturable intensity facilitates pulse splitting to achieve harmonic mode-locking.

Experimental results

The experimental schematic diagram of the Erbium-doped fiber ring cavity is shown in Fig. 5. The wavelength division multiplexer (WDM) of 980/1550 nm couples pump light with a wavelength of 974 nm into a gain fiber of 1.5 m. The type of gain fiber used is I-25(980/125) with a group velocity dispersion of 40 ps^2 km^{-1}. A polarization-independent isolator (PI-ISO) ensures unidirectional transmission of the laser and indicates that the mode-locking state in the ring cavity is due to the contribution of SA. The polarization state and the mode-locking state in the ring cavity are optimized by a three-ring type
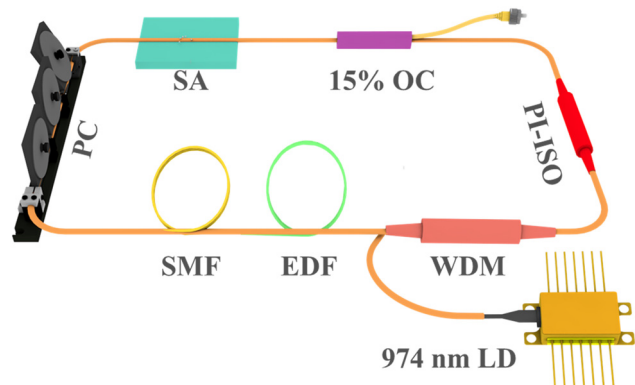
This journal is © The Royal Society of Chemistry and the Chinese Chemical Society 2024

Mater. Chem. Front., 2024, **8**, 1971–1980 | **1975**

Fig. 5 Schematic diagram of the mode-lcoked erbium-doped fiber laser.

polarization controller. The signal laser was output through a 15% coupler and measured by the optical spectrum analyzer (MS9740B, Anritsu), a 3 GHz InGaAs photodetector, a digital oscilloscope (MDO4104C, Tektronix), a radio frequency (RF) analyzer (R&S FPC1000), and an autocorrelator (FR-103XL).

Inserting the Fe-ZIF67 saturable absorber into the ring cavity, we carefully rotated the PC, and the CS mode-locking was achieved. Fig. 6(a) shows the optical spectrum of CS with a central wavelength of 1560.8 nm and a 3 dB spectral bandwidth of 2.6 nm. The Kelly sidebands are symmetrically distributed on either side of the central wavelength. Fig. 6(b) presents the mode-locking pulse train with a similar pulse intensity and pulse interval of 136.6 ns, corresponding to the length of the ring cavity of 28 m. The pulse width was measured by the autocorrelator, and the autocorrelation trace is shown in

Fig. 6(c). Fitting the trace with the sech^2 function, the pulse width was 1.23 ps, corresponding to the TBP (time-bandwidth product) was 0.393, which was slightly larger than the Fourier transform limit value (0.315), indicating that the pulse has a little chirp. To verify the stability of the mode-locking, we observed the radio frequency (RF) spectrum, as can be seen from Fig. 6(d), the central frequency was 7.31 MHz, which matched the pulse interval, indicating that the operation was in the fundamental frequency mode-locking state. Besides, the SNR of the laser can reach 50 dB, so the intracavity mode-locking state operated stably. Further increasing the pump power, the mode-locking operation was still maintained, and the optical spectra under different pump powers were recorded. We can see from Fig. 6(e) that the central wavelength was unchanged with the increase of the pump power, but the Kelly sidebands became apparent. With the increase of the pump power, the constructive interference between solitons and perturbed dispersive waves in the fiber laser cavity was enhanced, so the Kelly sideband became more obvious. What's more, the output power of the mode-locking operation under different pump power is depicted in Fig. 6(f). The output power increases linearly with the pump power, and the maximum output power is 3.152 mW at the pump power of 387 mW, corresponding to a single pulse energy of 0.43 nJ.

Carefully rotating the PC so that the intracavity birefringence was in the proper state, the phase relationship between the multiple solitons could be fixed, and the solitons were finally clustered together. When the pump power was kept at 387 mW, the solitons were tightly clustered together to form a large envelope, that is, a cluster of solitons was obtained.
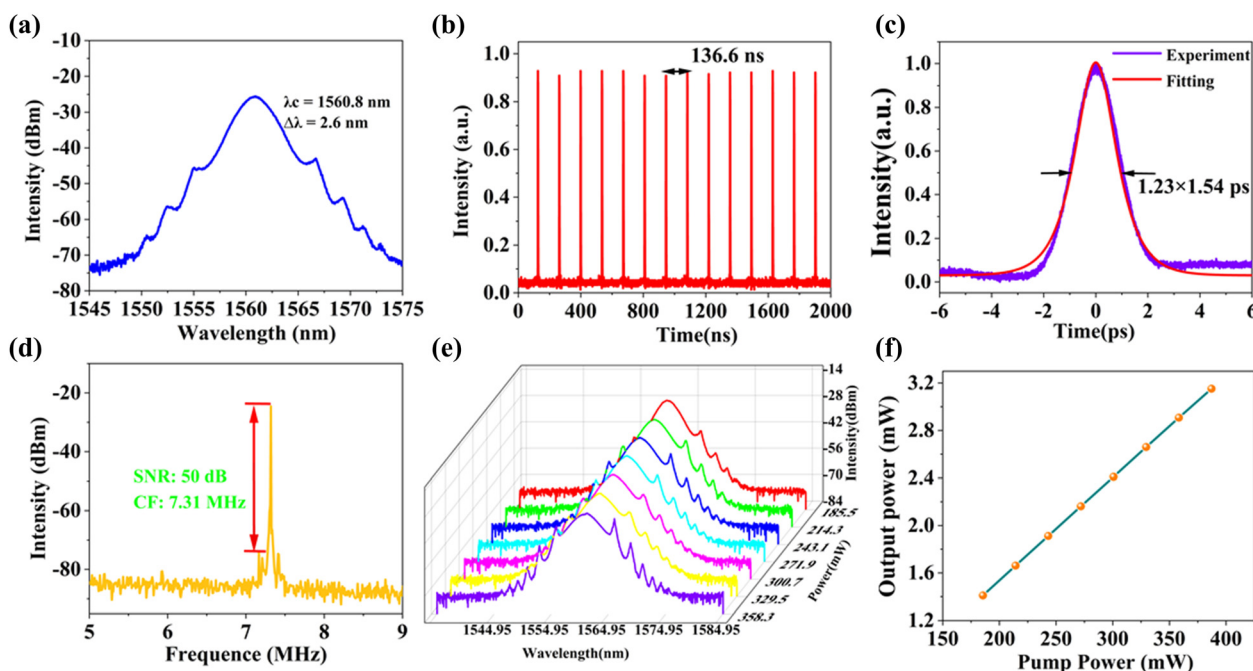

Fig. 6 (a) Optical spectrum of conventional soliton mode-locking; (b) oscilloscope tracking of the mode-locking pulse train; (c) autocorrelation trace with a sech^2 fitting; (d) the RF spectrum of mode-locking pulses; (e) spectral evolution at different pump powers; (f) output power at different pump power.
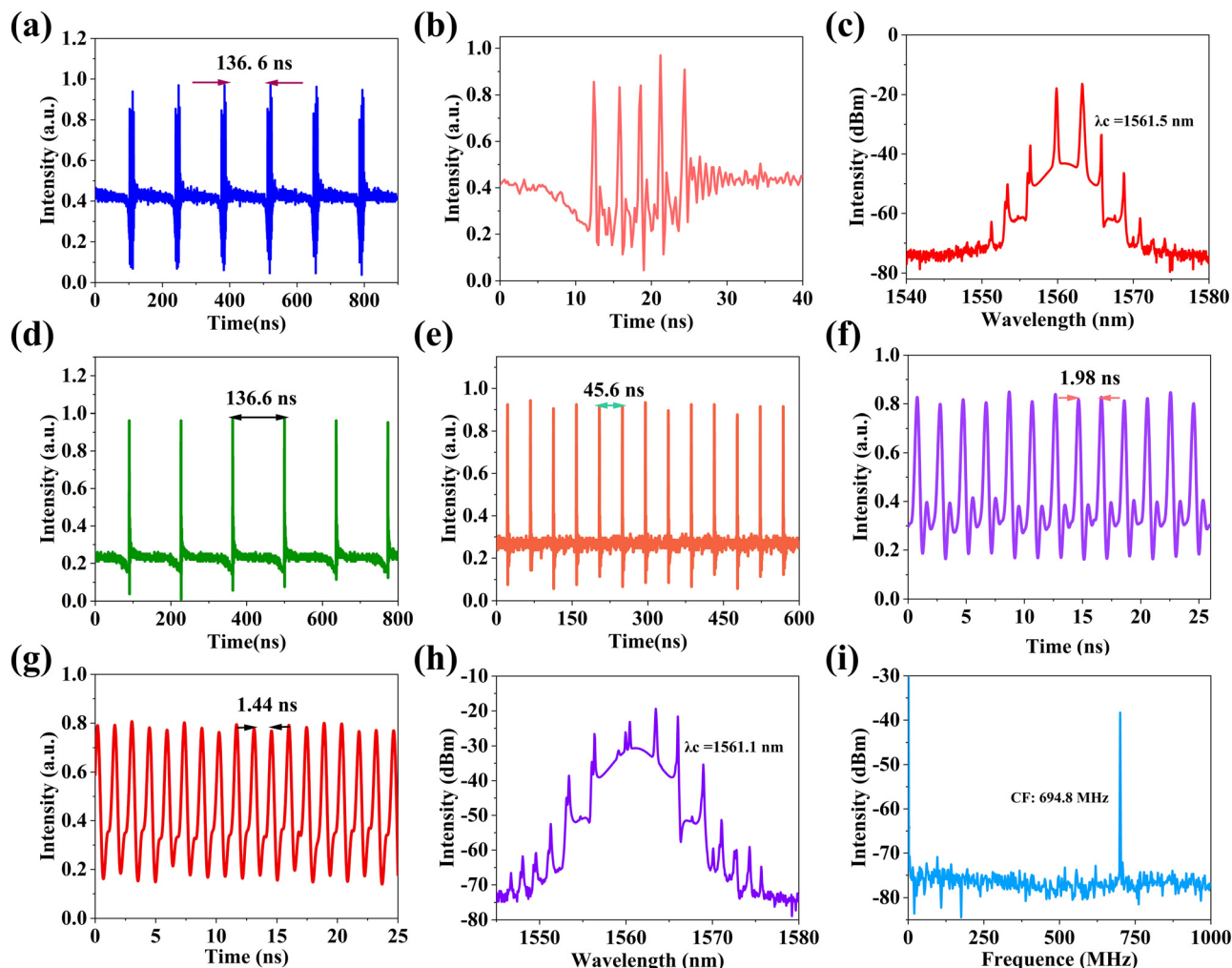
Fig. 7 (a) Oscilloscope trace of the soliton cluster; (b) single pulse cluster; (c) the optical spectrum of the soliton cluster; (d) fundamental frequency mode-locking pulse train; (e) third-order mode-locking pulse train; (f) 69th-order mode-locking pulse train; (g) 95th-order mode-locking pulse train; (h) the optical spectrum of 95th-order mode-locking; (i) the RF spectrum of 95th-order mode-locking.

Fig. 7(a) shows a sequence of soliton clusters displayed on an oscilloscope. The interval between soliton clusters is 136.6 ns, which is consistent with the pulse interval of CS mode-locking at the fundamental frequency. Fig. 7(b) is a single soliton cluster magnified in Fig. 7(a). The soliton cluster contains five pulses, varying in intensity and time interval. Fig. 7(c) shows the spectrum of the soliton cluster. There is continuous light at the top of the spectrum, which is the result of the interaction between the nonlinear effect of Fe-ZIF67 and the birefringence effect in the cavity. Compared with the spectrum of CS, the spectrum of the soliton cluster features dip-sidebands. The reason for dip-sideband formation can be attributed to the destructive interference and four-wave mixing of solitons and dispersive waves in the laser cavity. With the pump power still at 387 mW, we continue to adjust the PC, and we regain the CS mode-locking at the fundamental frequency, as shown in Fig. 7(d), the pulse interval is still 136.6 ns, but compared to the CS mode-locking pulse train in Fig. 6(b), we can find traces of pulses below the baseline, which may indicate that the pulse

is about to split. Surprisingly, without increasing the pump power, we only slightly changed the direction of the PC to achieve the pulse interval from 45.6 ns to 1.98 ns adjustable mode-locking operation, the corresponding repetition frequency of 21.93 MHz to 504.6 MHz, the corresponding harmonic order of 3 to 69. The 3rd and 69th-order harmonic mode-locking pulse sequences are shown in Fig. 7(e) and (f). By constantly adjusting the PC, we finally realized the 95th-order harmonic mode-locking with the minimum pulse interval of 1.44 ns, and the pulse train is shown in Fig. 7(g). The corresponding spectrum is shown in Fig. 7(h). The central wavelength of the mode-locking is 1561.1 nm, there is a continuous light component at the top of the spectrum, and the Kelly sideband is obvious on both sides. Fig. 7(i) provides the RF spectrum of 95th-order harmonic mode-locking, the center frequency is 694.8 MHz, corresponding to the mode-locking pulse interval of 1.44 ns, and the signal-to-noise ratio of mode-locking is about 40 dB, indicating that the mode-locking operation has excellent stability. Table 1 summarizes the mode-locking

Table 1 Comparison of output performance of pulsed fiber lasers based on ZIF-67, iron oxide, and other SAs

Material	λ (nm)	Integration method	Maximum repetition frequency (MHz)	Ref.
ZIF-67	1557.2	D-shape fiber	9.02	47
ZIF-67	1559.7	Ferrule	12.65	48
ZIF-8@ZIF-67	1565.6	Tapered fiber	7.29	49
rGO-ZIF-67	1529.8	Tapered fiber	5.53	50
Fe_3O_4	1572.4	Ferrule	2.81	51
Fe_3O_4	1595	Ex-TFG	15.84	52
Fe_3O_4	1558	Ferrule	37.32	53
PbTe	1569.9	Tapered fiber	6.25	54
γ-MnO_2	1561	Dual-core, pair-hole fiber	600	55
Cu_2O	1556.8	Tapered fiber	980	56
Bi_2O_2Te	1558.9	Tapered fiber	1780	57
Fe-ZIF-67	1561.1	Tapered fiber	694.8	This work

operation parameters based on some ZIF-67, iron oxides, and other materials as saturable absorbers. As can be seen from the table, at 1.5 μm, the mode-locking operation achieved based on ZIF-67 and iron oxides is the fundamental frequency, with a frequency of tens of MHz. By doping ZIF-67 with Fe, the mode-locking frequency was successfully increased to the order of several hundred MHz. The high repetition frequency laser has important applications in high-speed optical communication, spectroscopy, accurate measurement, and other fields. Table 1 also indicates that Fe-ZIF-67 has excellent saturable absorption effect, and provides a strategy to modify ZIF-67 with doping to achieve high repetition frequency mode-locking pulse output. In the future work, Fe-ZIF-67 can be combined with organic materials with excellent nonlinear optical properties,[58] and the parameters of the fiber cavity can be theoretically simulated,[59,60] and more advanced optoelectronics technology can be used,[61,62] to achieve a pulse fiber laser with better performance.[63]

Conclusions

In summary, we have demonstrated that crystalline ZIF-67 can be changed into amorphous Fe-ZIF-67 by doping of Fe elements and calcination. Then, the carrier dynamics of Fe-ZIF-67 and ZIF-67 were revealed by TAS. The variation of ΔA with the probe delay time can be attributed to three carrier dynamics processes. The amorphous Fe-ZIF-67 showed a lower photoinduced bleaching valley and higher photoinduced absorption peak than the crystalline ZIF-67. The nonlinear saturable absorption characteristics of Fe-ZIF-67 are studied by means of the twin-balanced detector system. These results show that Fe-ZIF-67 possesses an ultrafast optical response time and a very low saturable intensity. These excellent properties allow the Fe-ZIF-67 integrated SA to be inserted into the EDFL cavity, producing fundamental frequency mode-locking with a pulse width of 1.23 ps and 95th-order harmonic mode-locking with a repetition rate of 694.8 MHz. The finding indicates that amorphous Fe-ZIF-67 has great application potential in nonlinear optics and can be used as a preferred candidate for the development of advanced photonic devices.

Conflicts of interest

There are no conflicts to declare.

Notes and references

1 A. Greer, Metallic glasses, *Science*, 1995, **267**, 1947–1953.
2 G. Greaves and S. Sen, Inorganic glasses, glass-forming liquids and amorphizing solids, *Adv. Phys.*, 2007, **56**, 1–166.
3 T. Saragi, T. Spehr, A. Siebert, T. Fuhrmann-Lieker and J. Salbeck, Spiro compounds for organic optoelectronics, *Chem. Rev.*, 2007, **107**, 1011–1065.
4 T. Bennett, A. Goodwin, M. Dove, D. Keen, M. Tucker, E. Barney, A. Soper, E. Bithell, J. Tan and A. Cheetham, Structure and properties of an amorphous metal-organic framework, *Phys. Rev. Lett.*, 2010, **104**, 115503.
5 H. Sheng, H. Qu, B. Zeng, Y. Li, C. Xia, C. Li, L. Cao and B. Dong, Enriched Fe Doped on Amorphous Shell Enable Crystalline@Amorphous Core–Shell Nanorod Highly Efficient Electrochemical Water Oxidation, *Small*, 2023, **19**, 2300876.
6 T. Guo, L. Li and Z. Wang, Recent Development and Future Perspectives of Amorphous Transition Metal-Based Electrocatalysts for Oxygen Evolution Reaction, *Adv. Energy Mater.*, 2022, **12**, 2200827.
7 C. Rao, A. Cheetham and A. Thirumurugan, Hybrid inorganic-organic materials: a new family in condensed matter physics, *J. Phys.: Condens. Matter*, 2008, **20**, 159801.
8 G. Ferey, Some suggested perspectives for multifunctional hybrid porous solids, *Dalton Trans.*, 2009, 4400–4415.
9 A. Sapnik, I. Bechis, S. Collins, D. Johnstone, G. Divitini, A. Smith, P. Chater, M. Addicoat, T. Johnson, D. Keen, K. Jelfs and T. Bennett, Mixed hierarchical local structure in a disordered metal-organic framework, *Nat. Commun.*, 2021, **12**, 2062.
10 A. Sapnik, C. Sun, J. Laulainen, D. Johnstone, R. Brydson, T. Johnson, P. Midgley, T. Bennett and S. Collins, Mapping nanocrystalline disorder within an amorphous metal-organic framework, *Commun. Chem.*, 2023, **6**, 92.
11 T. Bennett and A. Cheetham, Amorphous Metal-Organic Frameworks, *Acc. Chem. Res.*, 2014, **47**, 1555–1562.
12 T. Bennett, P. Saines, D. Keen, J. Tan and A. Cheetham, Ball-Milling-Induced Amorphization of Zeolitic Imidazolate Frameworks (ZIFs) for the Irreversible Trapping of Iodine, *Chem. – Eur. J.*, 2013, **19**, 7049–7055.
13 C. Orellana-Tavra, E. Baxter, T. Tian, T. Bennett, N. Slater, A. Cheetham and D. Fairen-Jimenez, Amorphous metal-organic frameworks for drug delivery, *Chem. Commun.*, 2015, **51**, 13878–13881.

14 H. Wu, S. Huang, F. Ding, Y. Ma, Q. Zhai, Y. Ren, Y. Yang, L. Chen, S. Tang and X. Meng, Amorphous Bimetallic Metal-Organic Frameworks with an Optimized D-Band Center Enable Accelerating Oxygen Evolution Reaction, *J. Phys. Chem. C*, 2022, **126**, 19715–19725.

15 C. Liu, J. Wang, J. Wan, Y. Cheng, R. Huang, C. Zhang, W. Hu, G. Wei and C. Yu, Amorphous Metal-Organic Framework-Dominated Nanocomposites with Both Compositional and Structural Heterogeneity for Oxygen Evolution, *Angew. Chem., Int. Ed.*, 2020, **59**, 3630–3637.

16 H. Yang, X. He, F. Wang, Y. Kang and J. Zhang, Doping copper into ZIF-67 for enhancing gas uptake capacity and visible-light-driven photocatalytic degradation of organic dye, *J. Mater. Chem.*, 2012, **22**, 21849–21851.

17 J. Li, R. J. Kuppler and H. Zhou, Selective gas adsorption and separation in metal-organic frameworks, *Chem. Soc. Rev.*, 2009, **38**, 1477–1504.

18 L. Xin, D. Zhang, K. Qu, Y. Lu, Y. Wang, K. Huang, Z. Wang, W. Jin and Z. Xu, Zr-MOF-Enabled Controllable Ion Sieving and Proton Conductivity in Flow Battery Membrane, *Adv. Funct. Mater.*, 2021, **31**, 2104629.

19 Z. Zhan, Y. Jia, D. Li, X. Zhang and M. Hu, A water-stable terbium-MOF sensor for the selective, sensitive, and recyclable detection of Al3+ and CO32- ions, *Dalton Trans.*, 2019, **48**, 15231–15238.

20 O. Shekhah, J. Liu, R. A. Fischer and C. Woell, MOF thin films: existing and future application, *Chem. Soc. Rev.*, 2011, **40**, 1081–1106.

21 H. Bux, F. Liang, Y. Li, J. Cravillon, M. Wiebcke and J. Caro, Zeolitic Imidazolate Framework Membrane with Molecular Sieving Properties by Microwave-Assisted Solvothermal Synthesis, *J. Am. Chem. Soc.*, 2009, **131**, 16000.

22 U. Tran, K. Le and N. Phan, Expanding Applications of Metal-Organic Frameworks: Zeolite Imidazolate Framework ZIF-8 as an Efficient Heterogeneous Catalyst for the Knoevenagel Reaction, *ACS Catal.*, 2011, **1**, 120–127.

23 H. Jiang, B. Liu, T. Akita, M. Haruta, H. Sakurai and Q. Xu, Au@ZIF-8: CO Oxidation over Gold Nanoparticles Deposited to Metal-Organic Framework, *J. Am. Chem. Soc.*, 2009, **131**, 11302.

24 Y. Tian, C. Cai, X. Ren, C. Duan, Y. Xu, S. Gao and X. You, The silica-like extended polymorphism of cobalt (II) imidazolate three-dimensional frameworks: X-ray single-crystal structures and magnetic properties, *Chem. – Eur. J.*, 2003, **9**, 5673–5685.

25 R. Banerjee, A. Phan, B. Wang, C. Knobler, H. Furukawa, M. O'Keeffe and O. M. Yaghi, High-throughput synthesis of zeolitic imidazolate frameworks and application to CO_2 capture, *Science*, 2008, **319**, 939–943.

26 G. Greaves, F. Meneau, A. Sapelkin, L. Colyer, I. Gwynn, S. Wade and G. Sankar, The rheology of collapsing zeolites amorphized by temperature and pressure, *Nat. Mater.*, 2003, **2**, 622–629.

27 H. Pan, H. Chu, X. Wang, Y. Li, S. Zhao, G. Li and D. Li, Optical nonlinearity of zeolitic imidazolate framework-67 in the near-infrared region, *Mat. Chem. Front.*, 2020, **4**, 2081–2088.

28 B. Kafle, S. Acharya, S. Thapa and S. Poudel, Structural and optical properties of Fe-doped ZnO transparent thin films, *Ceram. Int.*, 2016, **42**, 1133–1139.

29 L. Wang, Y. Guan, X. Qiu, H. Zhu, S. Pan, M. Yu and Q. Zhang, Efficient ferrite/Co/porous carbon microwave absorbing material based on ferrite@metal–organic framework, *Chem. Eng. J.*, 2017, **326**, 945–955.

30 K. Nam, Y. Seon, P. Bandyopadhyay, J. Cho and S. Jeong, Porous nanofibers comprising hollow Co_3O_4/Fe_3O_4 nanospheres and nitrogen-doped carbon derived by Fe@ZIF-67 as anode materials for lithium-ion batteries, *Int. J. Energy Res.*, 2022, **46**, 8934–8948.

31 R. Fu, X. Wu, X. Wang, W. Ma, L. Yuan, L. Gao, K. Huang and S. Feng, Low-temperature hydrothermal fabrication of Fe_3O_4 nanostructured solar selective absorption films, *Appl. Surf. Sci.*, 2018, **458**, 629–637.

32 T. Yamashita and P. Hayes, Analysis of XPS spectra of Fe2+ and Fe3+ ions in oxide materials, *Appl. Surf. Sci.*, 2008, **254**, 2441–2449.

33 P. Bagus, C. Nelin, C. Brundle, B. Crist, N. Lahiri and K. Rosso, Combined multiplet theory and experiment for the Fe 2p and 3p XPS of FeO and Fe_2O_3, *J. Chem. Phys.*, 2021, **154**, 094709.

34 L. Kong, H. Chu, M. Xu, S. Xu, Z. Pan, S. Zhao and D. Li, Oxygen vacancy engineering of MOF-derived ZnO/Co_3O_4 nanocomposites for high harmonic mode-locking operation, *J. Mater. Chem. C*, 2022, **10**, 16564–16572.

35 D. Zhang, Z. Yang, Z. Wu and G. Dong, Metal-organic frameworks-derived hollow zinc oxide/cobalt oxide nanoheterostructure for highly sensitive acetone sensing, *Sens. Actuators, B*, 2019, **283**, 42–51.

36 S. Mo, Q. Zhang, S. Li, Q. Ren, M. Zhang, Y. Xue, R. Peng, H. Xiao, Y. Chen and D. Ye, Integrated Cobalt Oxide Based Nanoarray Catalysts with Hierarchical Architectures: In Situ Raman Spectroscopy Investigation on the Carbon Monoxide Reaction Mechanism, *ChemCatChem*, 2018, **10**, 3012–3026.

37 H. Chen, Z. Zhang, D. Hu, C. Chen, Y. Zhang, S. He and J. Wang, Catalytic ozonation of norfloxacin using Co_3O_4/C composite derived from ZIF-67 as catalyst, *Chemosphere*, 2021, **265**, 129047.

38 J. Huang, N. Dong, N. Mcevoy, L. Wang, H. Wang and J. Wang, Exciton-Like and Mid-Gap Absorption Dynamics of PtS in Resonant and Transparent Regions, *Laser Photon. Rev.*, 2022, **16**, 2100654.

39 J. Huang, N. Dong, N. Mcevoy, L. Wang, C. Coilean, H. Wang, C. Cullen, C. Chen, S. Zhang, L. Zhang and J. Wang, Surface-State Assisted Carrier Recombination and Optical Nonlinearities in Bulk to 2D Nonlayered PtS, *ACS Nano*, 2019, **13**, 13390–13402.

40 L. Wang, S. Zhang, J. Huang, Y. Mao, N. Dong, X. Zhang, I. Kislyakov, H. Wang, Z. Wang, C. Chen, L. Zhang and J. Wang, Auger-type process in ultrathin ReS_2, *Opt. Mater. Express*, 2020, **10**, 1092–1104.

41 H. Wang, C. Zhang and F. Rana, Surface Recombination Limited Lifetimes of Photoexcited Carriers in Few-Layer Transition Metal Dichalcogenide MoS_2, *Nano Lett.*, 2015, **15**, 8204–8210.

42 K. Zhang, Z. Jiang, J. Qiao, P. Lu, C. Qin, H. Yin, X. Du, W. Qin and X. Hao, Dredging photocarrier trapping pathways via "charge bridge" driven exciton-phonon decoupling enables efficient and photothermal stable quaternary organic solar cells, *Energy Environ. Sci.*, 2023, **16**, 3350–3362.

43 Y. Liang, X. Yuan, Z. Zeng, B. Zhu and Y. Gu, Strong interfacial interactions of ZnS/Cu-TCPP hybrids contribute to excellent nonlinear optical absorption, *Mater. Today Phys.*, 2022, **29**, 100920.

44 Y. Hu, H. Chu, X. Ma, Y. Li, S. Zhao and D. Li, Enhanced optical nonlinearities in Ti_3C_2 MXene decorated Fe_3O_4 nanocomposites for highly stable ultrafast pulse generation, *Mater. Today Phys.*, 2021, **21**, 100482.

45 L. Dong, H. Chu, Y. Li, S. Zhao and D. Li, Enhanced optical nonlinearity and ultrafast carrier dynamics of TiO_2/CuO nanocomposties, *Composites, Part B*, 2022, **237**, 109860.

46 N. Xu, P. Ma, S. Fu, X. Shang, S. Jiang, S. Wang, D. Li and H. Zhang, Tellurene-based saturable absorber to demonstrate large-energy dissipative soliton and noise-like pulse generations, *Nanophotonics*, 2020, **9**, 2783–2795.

47 M. Xu, H. Chu, Y. Hu, H. Pan, Z. Pan, S. Zhao and D. Li, Polyhedron ZIF-67 nanoparticles deposited on a D-shape fibre for stable soliton operation in an ultrashort fibre laser, *Mat. Chem. Front.*, 2022, **6**, 2729–2734.

48 P. Wang and C. Zhu, Passively Q-Switched and Mode-Locked Fiber Laser Based on a Zeolitic Imidazolate Framework-67 Saturable Absorber, *Front. Phys.*, 2022, **10**, 926344.

49 M. Xu, H. Chu, Z. Pan, H. Pan, S. Zhao and D. Li, Nonlinear optical features in core–shell ZIF-8@ZIF-67 for ultrashort pulse generation in Yb- and Er-doped fiber lasers, *Opt. Laser Technol.*, 2023, **164**, 109531.

50 M. An, Z. Pan, X. Li, W. Wang, C. Jiang, G. Li, P. Guo, H. Lu, Y. Han, X. Chen and Z. Zhang, Co-MOFs as Emerging Pulse Modulators for Femtosecond Ultrafast Fiber Laser, *ACS Appl. Mater. Interfaces*, 2022, **14**, 53971–53980.

51 P. Cheng, Y. Du, M. Han and X. Shu, Mode-locked and Q-switched mode-locked fiber laser based on a ferroferric-oxide nanoparticles saturable absorber, *Opt. Express*, 2020, **28**, 13177–13186.

52 H. Wang, F. Zhao, Z. Yan, X. Hu, K. Zhou, T. Zhang, W. Zhang, Y. Wang, W. Zhao, L. Zhang and C. Sun, Excessively tilted fiber grating based Fe_3O_4 saturable absorber for passively mode-locked fiber laser, *Opt. Express*, 2019, **27**, 15693–15700.

53 N. Li, H. Jia, J. X. Liu, L. H. Cui, Z. X. Jia, Z. Kang, G. Qin and W. Qin, Fe_3O_4 nanoparticles as the saturable absorber for a mode-locked fiber laser at 1558 nm, *Laser Phys. Lett.*, 2019, **16**, 065102.

54 X. Li, W. Xu, Y. Wang, X. Zhang, Z. Hui, H. Zhang, S. Wageh, O. A. Al-Hartomy and A. G. Al-Sehemi, Optical-intensity modulators with PbTe thermoelectric nanopowders for ultrafast photonics, *Appl. Mater. Today*, 2022, **28**, 101546.

55 X. Li, X. Huang, Y. Han, E. Chen, P. Guo, W. Zhang, M. An, Z. Pan, Q. Xu, X. Guo, X. Huang, Y. Wang and W. Zhao, High-performance γ-MnO_2 dual-core, pair-hole fiber for ultrafast photonics, *Ultrafast Sci.*, 2023, **3**, 0006.

56 X. Li, J. Feng, W. Mao, F. Yin and J. Jiang, Emerging uniform Cu_2O nanocubes for 251st harmonic ultrashort pulse generation, *J. Mater. Chem. C*, 2020, **8**, 14386–14392.

57 Z. Hui, X. Bu, Y. Wang, D. Han, J. Gong, L. Li, X. Li and S. Yan, Bi_2O_2Te nanosheets saturable absorber-based passive mode-locked fiber laser: from soliton molecules to harmonic soliton, *Adv. Opt. Mater.*, 2022, **10**, 2201812.

58 C. Zhang, X. Li, E. Chen, H. Liu, P. P. Shum and X. Chen, Hydrazone organics with third-order nonlinear optical effect for femtosecond pulse generation and control in the L-band, *Opt. Laser Technol.*, 2022, **151**, 108016.

59 X. Li, X. Huang, E. Chen, Y. Zhou and Y. Han, Dissipative-soliton-resonance and evolution in an all-normal dispersion Er-doped fiber laser, *Opt. Laser Technol.*, 2022, **156**, 108592.

60 M. Guan, D. Chen, S. Hu, H. Zhao, P. You and S. Meng, Theoretical insights into ultrafast dynamics in quantum materials, *Ultrafast Sci.*, 2022, 9767251.

61 Q. Jin, E. Yiwen, S. Gao and X. Zhang, Preference of subpicosecond laser pulses for terahertz wave generation from liquids, *Adv. Photonics*, 2020, **2**, 015001.

62 Z. Zhang, J. Zhang, Y. Chen, T. Xia, L. Wang, B. Han, F. He, Z. Sheng and J. Zhang, Bessel terahertz pulses from superluminal laser plasma filaments, *Ultrafast Sci.*, 2022, 9870325.

63 Y. Song, Z. Wang, C. Wang, K. Panajotov and H. Zhang, Recent progress on optical rogue waves in fiber lasers: status, challenges, and perspectives, *Adv. Photonics*, 2020, **2**, 024001.